Near-field ptychography using lateral and longitudinal shifts

2015 New J. Phys. 17 073033

(http://iopscience.iop.org/1367-2630/17/7/073033)

New Journal of Physics
The open access journal at the forefront of physics

Deutsche Physikalische Gesellschaft DPG
IOP Institute of Physics

Published in partnership with: Deutsche Physikalische Gesellschaft and the Institute of Physics

OPEN ACCESS

RECEIVED
13 March 2015

REVISED
19 June 2015

ACCEPTED FOR PUBLICATION
6 July 2015

PUBLISHED
31 July 2015

PAPER

Near-field ptychography using lateral and longitudinal shifts

A-L Robisch[1], **K Kröger**[1], **A Rack**[2] **and T Salditt**[1]

[1] Institut für Röntgenphysik, Georg-August-Universität Göttingen, Friedrich-Hund-Platz 1, Göttingen, Germany
[2] European Synchrotron Radiation Facility, 38043 Grenoble Cedex, France

E-mail: arobisc@gwdg.de **and** tsaldit@gwdg.de

Keywords: phase retrieval, ptychography, holography

Supplementary material for this article is available online

Abstract

Image reconstruction of in-line holography depends crucially on the probing wave front used to illuminate an object. Aberrations inherent to the illumination can mix with the features imposed by the object. Conventional raw data processing methods rely on the division of the measured hologram by the intensity profile of the probe and are not able to fully eliminate artifacts caused by the illumination. Here we present a generalized ptychography approach to simultaneously reconstruct object and probe in the optical near-field. Combining the ideas of ptychographic lateral shifts of the object with variations of the propagation distance by longitudinal shifts, simultaneous reconstruction of object and probe was achieved equally well for a highly aberrated and a mildly disturbed probe without the need for an additional wave front diffuser. The method overcomes the image deterioration by a non-ideal probe and at the same time any restrictions due to linearization of the object's transmission function or the Fresnel propagator. The method is demonstrated experimentally using visible light and hard x-rays, in both parallel beam and cone beam geometry, which is relevant for high resolution x-ray imaging. It also opens up a new approach to characterize extended wave fronts by phase retrieval.

1. Introduction

In-line holography is a well-known technique to reconstruct the complex-valued transmission function $o(x, y)$ of a semi-transparent or transparent object from the (near-field) intensity distribution of the propagated exit wave $\psi(x, y, z)$, which is recorded at some distance z behind the object in the detection plane [1]. Applications are particularly important in the x-ray spectral range, providing full-field phase contrast images without lenses [2–4]. Nanoscale resolution can be achieved by geometric magnification of the hologram, if a (quasi-)spherical wave is used as probing wave front p for the illumination of the object [2, 5]. Over the last few decades, advanced phase retrieval algorithms have been devised to suppress the artifacts encountered in simple holographic reconstruction based on back propagation of the measured hologram [6–8]. These rely either on: (1) linearization of the object's transmission function o using the contrast-transfer function (CTF) for a sample with weakly varying phase [4]; (2) linearization of the propagator [9, 10] as in algorithms based on the transport-of-intensity equation (TIE); (3) a well-known compact support [11]; (4) a coupling between the object's dispersion and absorption properties (single material assumption) [12].

Two major limitations restrict the applicability of in-line holographic imaging and microscopy: first, restrictive assumptions about the sample such as the linearizations mentioned above; second, idealizations with respect to the probe p which is generally assumed to be a perfect plane or spherical wave [13, 14]. Here we overcome both limitations by introducing a data recording and phase retrieval scheme which uses lateral and longitudinal shifts of the object in the beam to simultaneously reconstruct o and p without further constraints or restrictions. This approach increases the diversity in the data by combining the advantages of longitudinal shifts, as introduced by Cloetens *et al* in the framework of linearized CTFs [4], with the simultaneous ptychographic reconstruction of probe and object based on lateral shifts with overlap as introduced in [15–17]. Combining

lateral and longitudinal shifts to enhance phase diversity has already been introduced by Putkunz *et al*, who achieved superior reconstruction when the object is scanned in and around the focal plane of a compact probe [18]. In this work, we extend this idea by generalizing the concept to simultaneous reconstruction and to the extended wavefronts typically used for propagation imaging, i.e. in contrast to [18] the probe does not have to be compact.

The proposed scheme also overcomes the necessity for a wave front diffuser, which has so far been inevitable for generalizing ptychographic coherent diffractive imaging (PCDI) algorithms from the typical far-field case with a compact probe [15–17] to the near-field setting with extended wave fronts [19]. The advantage is that direct information about the probe (unperturbed by a diffuser) can be reconstructed.

Importantly, the generalized longitudinal ptychography approach (LPCDI) presented here does not need an *a priori* known or *a priori* reconstructed probe as in [18, 20], nor does it rely on any special properties of the probe in the pupil or on a focal plane to reconstruct p from intensity data [18, 21]. In fact, not even a separate recording of the probe (empty beam image/flat field) as in [22] is needed. At the same time, the proposed scheme allows for quantitative reconstruction of optically thick, extended and/or multi-component samples, i.e. for a general index of refraction $n = 1 - \delta + \mathrm{i}\beta$. The method is demonstrated first for visible light holography using a standard optical bench, after that for parallel beam phase contrast x-ray imaging without magnification, and finally for a cone beam setup enabling nanoscale resolution.

2. Theoretical background

LPCDI uses essentially two constraints for the reconstruction of object and probe: a magnitude constraint applied to the propagated exit wave by projection onto the near-field intensity distribution measured in the detector plane, and a separability constraint, which requires the exit wave ψ behind the object to be a product of the object's transmission function o and the (extended) probe p

$$\psi_j^{(i)^k} = o^{(i)^k}\, p_j^k = D_{\Delta_{1,j}}\left[p_1^k\right] S^{(1\to i)}\left[o^{(1)^k}\right]. \tag{1}$$

Upper indices (i) denote lateral shifts, upper indices k refer to the kth iteration of the algorithm, and lower indices represent translations along the optical axis.

The operator $S^{(i\to j)}$ shifts the object $o^{(i)}(\vec{r}) = o(\vec{r} + \vec{r}^{(i)})$ from the (lateral) position i to the (lateral) position j:

$$o^{(j)}\left(\vec{r}\right) = S^{(i\to j)}\left(o^{(i)}\left(\vec{r}\right)\right) = o\left(\vec{r} + \vec{r}^{(i)} + \left(\vec{r}^{(j)} - \vec{r}^{(i)}\right)\right) = o\left(\vec{r} + \vec{r}^{(j)}\right), \tag{2}$$

where $\vec{r}^{(i)}$ and $\vec{r}^{(j)}$ are the vectors pointing to the center of mass of the object at position i and j, respectively. The shift operator $S^{(i\to j)}$ shall always act on the transmission function of the object, not on the probe; hence

$$S^{(i\to j)}\left(\psi_j^{(i)}\right) = S^{(i\to j)}\left(o^{(i)}\right)p_j = \psi_j^{(j)}. \tag{3}$$

The Fresnel near-field propagator $D_{\Delta_{a,b}}[\psi_a]$ formulated as a convolution [6] propagates a complex valued optical field from defocus position a to defocus position b along the optical axis

$$D_{\Delta_{a,b}}[\psi_a] = \mathcal{F}^{-1}\left[\mathcal{F}[\psi_a]\,\exp\left\{-\frac{\mathrm{i}\Delta_{a,b}}{2k}\left(q_x^2 + q_y^2\right)\right\}\right], \tag{4}$$

with $\mathcal{F}$ and $\mathcal{F}^{-1}$ denoting the Fourier transform and the inverse Fourier transform, q_x, q_y the reciprocal coordinates, $k = \frac{2\pi}{\lambda}$ the wave number (with wavelength λ), and $\Delta_{a,b}$ the distance between the (longitudinal) position a and the (longitudinal) position b. The magnitude constraint applied to the reconstructed exit wave $\psi_j^{(i)^k}$ can then be written as

$$P_M\left[\psi_j^{(i)^k}\right] = D_{-\Delta_{j,\mathrm{det}}}\left[\frac{D_{\Delta_{j,\mathrm{det}}}\left[\psi_j^{(i)^k}\right]}{\left|D_{\Delta_{j,\mathrm{det}}}\left[\psi_j^{(i)^k}\right]\right|}\sqrt{I_j^{(i)}}\right], \tag{5}$$

where $I_j^{(i)}$ are the measured intensities at the detector and the index det indicates the detection plane. The magnitude constraint feeds in the measured data. From equation (5) it can be seen that this is accomplished by replacing the reconstructed amplitudes at the position of the detector by the measured ones while keeping the reconstructed phase information.

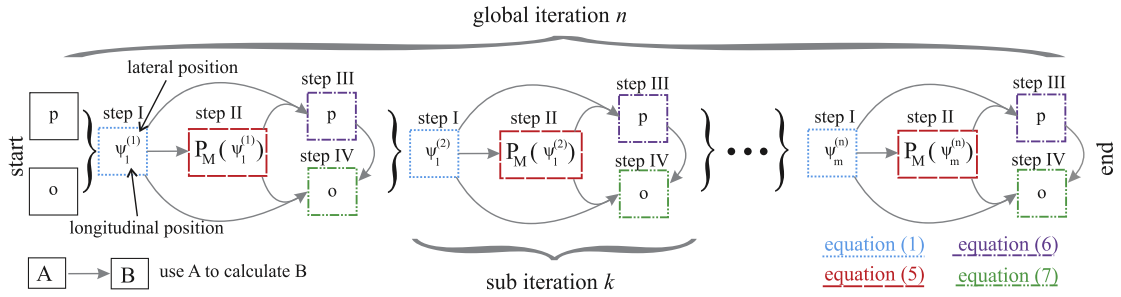

Figure 1. Sketch of one iteration of the near-field ptychographic phase retrieval algorithm. Equation labels refer to the equations given in the main text.

Next, probe and object are separated by

$$p_1^{k+1} = p_1^k + \alpha D_{-\Delta_{1,j}}\left[\frac{\left(P_M\left[\psi_j^{(i)k}\right] - \psi_j^{(i)k}\right) S^{(1\to i)}\left[o^{(1)k}\right]^*}{|S^{(1\to i)}\left[o^{(1)k}\right]|^2}\right], \tag{6}$$

and

$$o^{(1)k+1} = S^{(i\to 1)}\left[S^{(1\to i)}\left[o^{(1)k}\right] + \beta\frac{\left(P_M\left[\psi_j^{(i)k}\right] - \psi_j^{(i)k}\right) D_{\Delta_{1,j}}\left[p_1^{k+1}\right]^*}{|D_{\Delta_{1,j}}\left[p_1^{k+1}\right]|^2}\right] \tag{7}$$

respectively. The complex conjugate is indicated by *. In this formulation, updates for the probe take place at defocus position 1. The parameters α and β (both $\in[0,\ 1]$) combine the previous with the new guess of the probe and the object. Equation (6) can be interpreted in an intuitive way: noting that $|S^{(1\to i)}\left[o^{(1)k}\right]|^2 = S^{(1\to i)}\left[o^{(1)k}\right]S^{(1\to i)}\left[o^{(1)k}\right]^*$, the division by $|S^{(1\to i)}\left[o^{(1)k}\right]|^2$ combined by the multiplication by $S^{(1\to i)}\left[o^{(1)k}\right]^*$ is similar to the division by $S^{(1\to i)}\left[o^{(1)k}\right]$. Assuming that $P_M\left[\psi_j^{(i)k}\right]$ and $\psi_j^{(i)k}$ can be formulated as a product of object and probe, in equation (6)only the component referring to the probe is left. Equation (6) is a relaxed update of the probe assuming the corresponding exit wave to be a mixture of the previously guessed $\psi_j^{(i)k}$ and $P_M\left[\psi_j^{(i)k}\right]$, and similarly for the object, see equation (7). One iteration consists of m sub-iterations, where m is the number of recorded holograms, and is schematically depicted in figure 1. This algorithm is related to the ePIE method [17, 23]. Finally, to correct errors in propagation distances, automatic focussing similar to [24] can be applied during phase retrieval.

Near-field ptychography is initialized by a homogeneous amplitude and phase distribution for object and probe. Where a measured intensity pattern of the probe is available, one can equally use a back-propagated version of this intensity pattern as starting guess for the probe. Convergence can be monitored by calculating the difference between reconstructed and measured holograms, the difference between the object/the probe in successive iterations and by visual inspection of the current reconstruction during the phase retrieval process. In particular, a reconstruction is considered to be successful, when no twin image components [25], (see footnote 3) are visible in object and probe. The number of iterations needed for convergence depends on the specific experiments and the number of recorded holograms. The reconstructions presented here were achieved in about 20 global iterations. Furthermore, from a technical point of view, when deciding on the positions of the object with respect to the detector, it is important to ensure sufficient sampling of the near-field propagator [26]. Equation (4) is properly sampled, if

$$1 \geqslant \frac{\lambda\Delta_{a,b}}{Nd_x^2} \text{ and } 1 \geqslant \frac{\lambda\Delta_{a,b}}{Md_y^2}, \tag{8}$$

where N and M are the number of pixels in the horizontal and vertical directions; d_x and d_y are the respective pixel sizes. Either the distance $\Delta_{a,b}$ or the size of the field of view $Nd_x \times Md_y$ has to be chosen such that the conditions given in equation (8) are fulfilled.

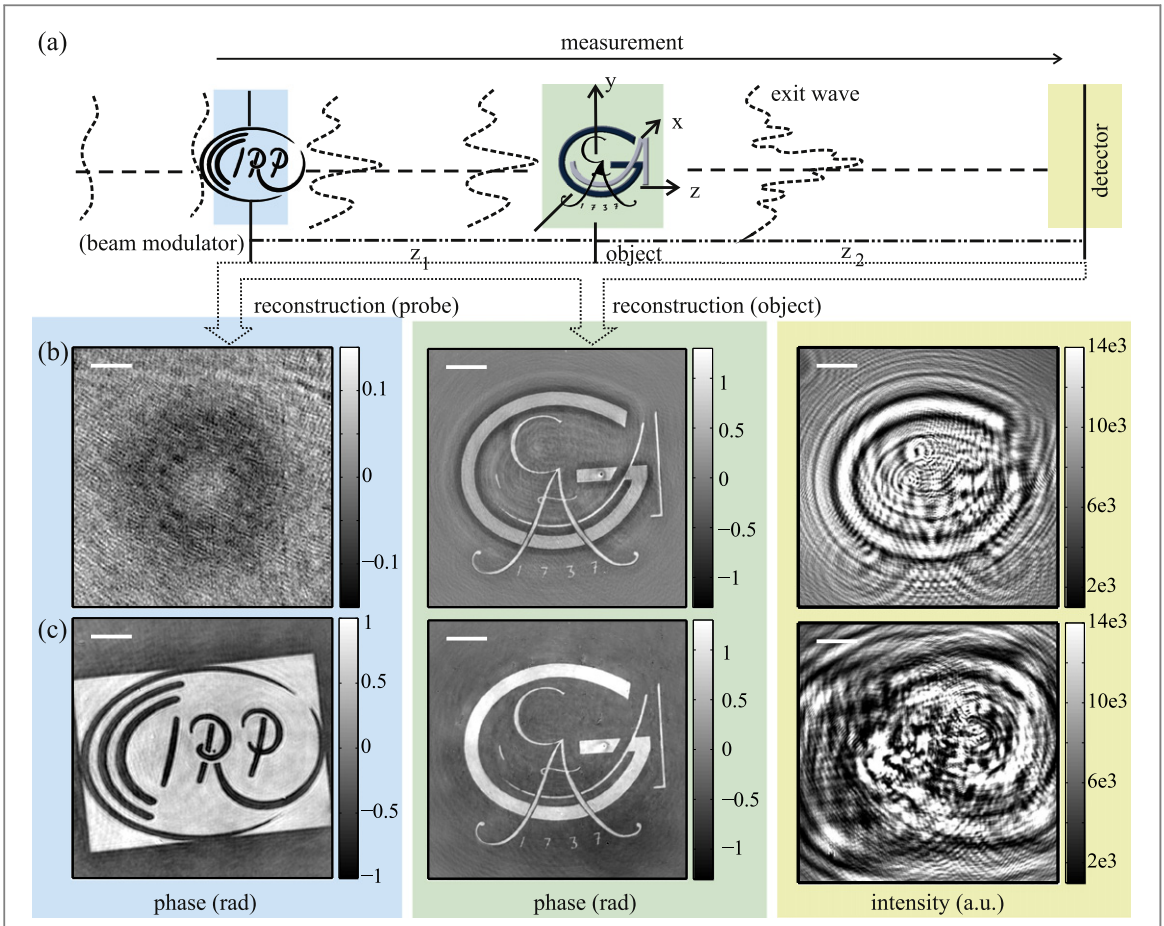

Figure 2. Visible light experiments. (a) Optical scheme for generalized near-field ptychography with simultaneous reconstruction of probe and object. The object can be shifted along (z) and perpendicular (x, y) to the optical axis. (b) Reconstruction of probe (phase) and object (phase) as well as an exemplary hologram. (c) Reconstruction of probe (phase) disturbed by an additional test pattern and object (phase) as well as an exemplary hologram. Colors define different positions along the optical axis. Scale bars denote 0.5 mm.

3. Experiments

The optical concept and phase retrieval algorithm were demonstrated in three different experimental setups, the first using a standard optical test bench with a HeNe-laser, followed by two experiments at synchrotron beamlines using hard x-rays in a parallel and a magnifying cone beam geometry, respectively.

For the visible light in-line holography experiment, a coherent, monochromatic, extended parallel beam probe was generated by coupling the laser beam (wavelength 633 nm) to a monomode optical fiber connected to a collimator (model 60FC-L-0-M60–33, Schäfter+Kirchhoff, Germany) with numerical aperture NA = 0.14. For intentional beam modulation, a test pattern (photoresist on glass with logo 'IRP') was inserted into the beam behind the collimator (modulation plane), see figure 2(a). The object (photoresist on glass with logo 'GAU') was positioned by a motorized *xyz*-stage at a variable distance 13 cm $\leqslant z_1 \leqslant$ 19.4 cm behind the fixed modulation plane, at distance 4.8 cm $\leqslant z_2 \leqslant$ 6.4 cm in front of the stationary CCD detector (CoolSnap Myo, Photometrics, USA). Holograms of the object were recorded as detailed in table 1, and as shown (illustrative examples) in figure 2 (right column) for the case of (b) the native (non-modulated) probe and (c) the modulated probe. The reconstructed phases of the probe (left column) and the object (center column) demonstrate phase retrieval with very high image quality for both cases, i.e. a weakly and a strongly modulated probe. Both logos (representing object and beam modulator) can be reconstructed simultaneously with perfect separability of features. Further details are given in[3].

The reconstruction of the probe modulated by the 'IRP'-structure precisely matches expectations by revealing the beam modulating object. For the native (unmodulated) probe shown in figure 2(b), it is not *a priori* clear what to expect. We therefore analyzed the reconstructed phase front in terms of optical Zernike polynomials. Motivated by the radial symmetry of the reconstructed phase, which exhibits a torus shape (in addition to high frequency noise), we first performed a low pass filtering step, followed by angular averaging (see

[3] See supplemental material at stacks.iop.org/njp/17/073033/mmedia for more detailed information on methods and procedures.

Table 1. Parameters for visible light in-line holography. Fresnel numbers $F_{10} = a^2/z\lambda$ are defined by a characteristic size of $a = 10\Delta d$, where Δd is the pixel size and λ is the wavelength.

object	photoresist (1.4 μm) on glass
beam modulation	no/photoresist (1.4 μm) on glass
geometry	parallel beam
wavelength [nm]	633
pixel size [μm]	4.54
number of pixels	1940×1460
accumulation time [ms]	10×6
sample–detector distances[cm]	6.52, 6.12, 5.69, 5.29, 4.87
F_{10}	0.050, 0.053, 0.057, 0.062, 0.067
# holograms	80 (5 defocus planes, each with 16 lateral shifts)
image corrections	dark image, faulty pixel mask
[mm]	0.85(h), 0.68(v)

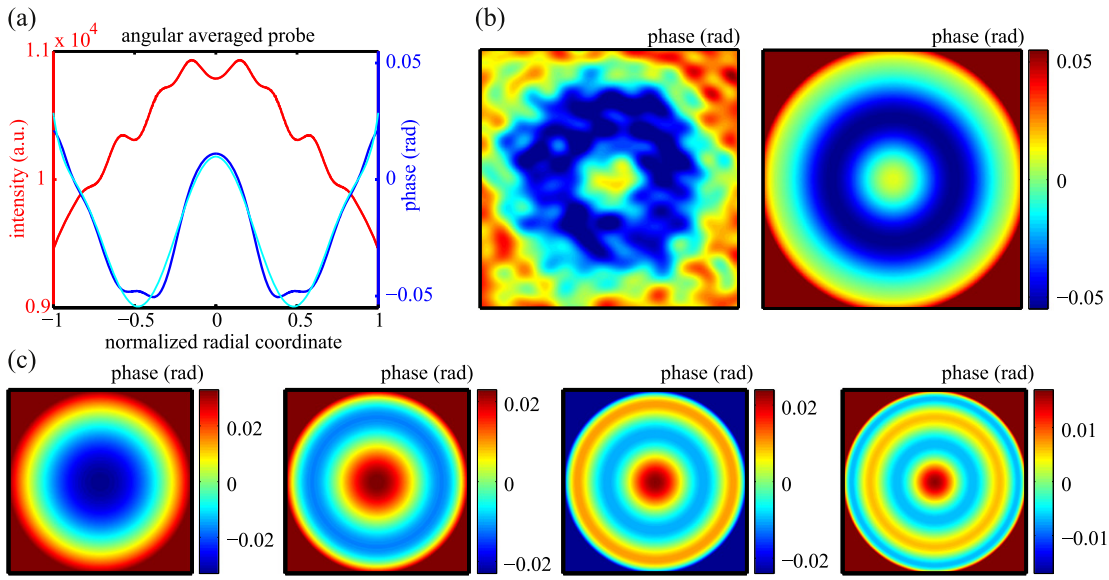

Figure 3. (a) Low pass filtered and angular averaged profile of the reconstructed probe depicted in figure 2(b). Red curve: Intensity profile; dark blue curve: phase profile; light blue curve: fitted linear combination of radial Zernike polynomials. (b) Low pass filtered phase profile in two dimensions along with the two dimensional representation of the fit provided in (a). (c) Single radial Zernike components with their respective weights. Their summation is shown in the right image of (b).

figure 3(a) and left image in (b)). The resulting profile is well fitted by a linear combination of four radial Zernike polynomials with radial coordinate ρ [27]

$$f(\rho) = a + b \cdot R_2^0(\rho) + c \cdot R_4^0(\rho) + d \cdot R_6^0(\rho) + e \cdot R_8^0(\rho) \tag{9}$$

with

$$R_2^0(\rho) = 2\rho^2 - 1, \tag{10a}$$

$$R_4^0(\rho) = 6\rho^4 - 6\rho^2 + 1, \tag{10b}$$

$$R_6^0(\rho) = 20\rho^6 - 30\rho^4 + 12\rho^2 - 1, \tag{10c}$$

$$R_8^0(\rho) = 70\rho^8 - 140\rho^6 + 90\rho^4 - 20\rho^2 + 1, \tag{10d}$$

as depicted in figure 3(a) where the dark blue curve shows the filtered, reconstructed phase and the light blue curve shows the corresponding linear combination of radial Zernike polynomials. Figure 3(b) shows the fitted phase profile in two dimensions (right image) next to the filtered reconstruction (left image). Finally in figure 3(c) the single components of equation (9) weighted by the prefactors b, c, d, e are shown. Hence, the reconstructed phase profile in figure 2(b) reveals mild spherical aberrations of the beam collimating lens.

Table 2. Setup for x-ray holography (ESRF/ID19).

object	W (3 μm)
beam modulation	no
geometry	parallel beam
wavelength [nm]	0.066
pixel size [μm]	0.70
number of pixels	2048×2048
accumulation time [s]	0.1
sample–detector distances [cm]	87.67, 87.37, 87.07, 86.77
F_{10}	0.842, 0.845, 0.848, 0.851
# holograms	64 (4 defocus planes, each with 16 lateral shifts)
[mm]	0.21(h), 0.21(v)

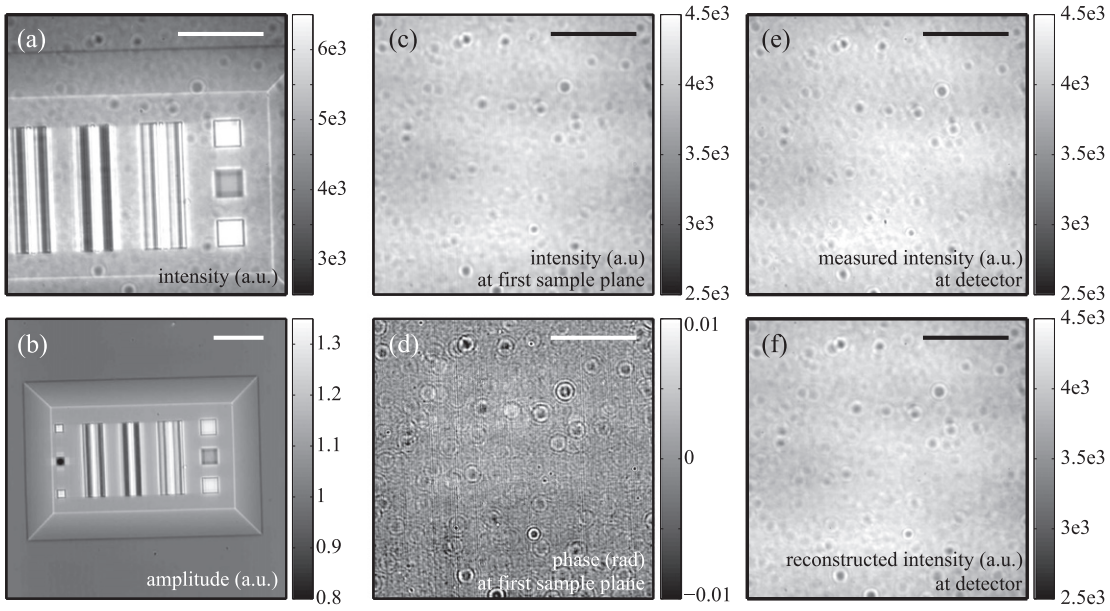

Figure 4. (a) An exemplary hologram recorded at ID19/ESRF. (b) Reconstructed amplitude of the object. (c) Reconstructed intensity of the probe at 87.7 cm upstream the detector. (d) Reconstructed phase of the probe at 87.7 cm upstream of the detector. (e) Measured intensity profile of the probe. (f) Reconstructed intensity profile of the probe at the detector. Scale bars denote 0.3 mm.

Next, generalized ptychographic phase retrieval for the important case of full-field phase contrast radiography is demonstrated. Experiments were performed using the pink beam mode with the first harmonic centered at photon energy $E = 18.77$ keV at the insertion device beam line ID19/ESRF [28], well known for seminal developments and applications of phase contrast x-ray imaging (x-ray propagation imaging) [4]. Again, the goal of the experiment was to demonstrate that the native probe of the beamline can be reconstructed simultaneously with the object, overcoming the restrictions inherent in the conventional empty beam corrections. Near-field images of a tungsten test pattern (3μm optical thickness) were recorded, translating the object at variable distances $z \in$ [86.8 cm, 87.7 cm] with respect to the stationary detector; see table 2 for all experimental parameters. For high resolution x-ray detection, a $Gd_3Ga_5O_{12}$:Eu single-crystal scintillator of 10 μm thickness with an optical microscope of $\times$20 magnification (NA = 0.4) and a fast read-out CCD (FReLoN2k, ESRF) was used [29].

The results are shown in figure 4. The exemplary near-field image (a) recorded in the direct contrast regime ($F_{10} = 0.842$) shows some near-field speckles [30]. These artifacts are completely removed in the reconstructed object function $|o|$ (b), which is obtained along with the complex-valued probe (c) and (d). A distinct separation of object and probe is thus achieved. The measured intensity profile of the probe (figure 4(e))-though not used during phase retrieval—compares well with the reconstructed intensity profile (figure 4(f))-validating the reconstruction of the probe.

In the following, the reconstruction of o and p is demonstrated for the important case of x-ray propagation in cone beam geometry. By geometric divergence of the illuminating probe, a near-field image of a nano-scale

Table 3. Setup for x-ray holography (DESY/P10)

object	Au+Ti (205 nm + 3 nm)
beam	
modulation	no
geometry	cone beam
wavelength [nm]	0.157
eff.pixel size [nm]	19.1, 19.2, 19.8, 20.4, 21.0, 21.7, 22.3
number of pixels	1920×1080
accumulation time [s]	2×3
focus–detector distance [m]	5.13
focus–detector distance [mm]	15.00, 15.04, 15.46, 15.96, 16.45, 16.96, 17.45
eff. F_{10}	15.6e − 3, 15.7e − 3, 16.1e − 3, 16.6e − 3, 17.2e − 3, 17.7e − 3, 18.2e − 3
# holograms	14 (7 defocus planes, 2 exposures each)
[μm]	1.4

object can be magnified to macroscopic detector size [2]. The required x-ray nano-focusing to a quasi-point source often leads to significant probe aberrations, which make simultaneous reconstruction particularly desirable for this case. To this end, the generalized near-field ptychography was adapted to account for different magnifications of object and probe, as detailed in (see footnote 3). According to the Fresnel scaling theorem [6], the magnifying cone beam geometry is equivalent to the parallel beam case, up to a variable transformation, which reduces the pixel size according to the geometric magnification $M = \frac{z_1 + z_2}{z_1}$, and changes the propagation distance to an effective length $z_{\text{eff}} = \frac{z_2}{M}$. Here z_1 is the distance between the focal plane and the sample plane, and z_2 is the distance between the sample plane and the detector plane (see also footnote 3). Magnifying cone beam x-ray holography was performed using the GINIX-setup of beamline P10/DESY [31, 32], at photon energy $E = 7.9$ keV. The undulator beam was focused by a Kirkpatrick–Baez mirror system onto an x-ray waveguide consisting of a lithographically defined air channel in silicon (91 nm × 70 nm × 1 mm) [33], to achieve a nearly perfect (coherent and mode filtered) probe for x-ray holography with nanoscale resolution [10, 34, 35].

The minimal distance z_1 between waveguide and sample ('IRP'-logo test chart made of 205 nm gold and 3 nm titanium) was 1.5 cm, resulting in a magnification of $M = 342$. The sample was then shifted downstream within an interval of 2.5 mm to seven positions along the optical axis, with lateral translation, and at constant distance $z_1 + z_2 = 5.13$ m from the fiber-coupled CCD detector (sCMOS, Photonic Science, UK), equipped with a scintillator (15 μm GdOS:Tb), see table 3 for further experimental parameters.

Figure 5 shows an exemplary hologram (with effective Fresnel number defined for a typical structure size of 10 pixels $F_{10} = 15.6\text{e}{-3}$) of the test pattern in the waveguide beam (a), along with the corresponding reconstructions of the object's amplitude (b) and phase (c), as well as the complex wave guide probe (d, e). To speed up convergence, twin image artifacts were suppressed during the first iterations of phase retrieval similar to the method proposed in [36]. The example shows that high quality reconstructions of o can be obtained in this highly holographic and magnifying regime without any support constraint as in [11], or regularization parameters to reduce the effect of zeros in the CTF [6]. At the same time the probe reconstruction proves that the wave front of the beam exiting the wave guide is well described by a spherical wave with a Gaussian envelope. Again the measured intensity (figure 5(f)) and the reconstructed intensity of the probe (figure 5(g)) agree well. Note that the measured flat field is of slightly lower intensity, because the waveguide slowly drifted during the measurement.

This experiment demonstrates that LPCDI can reconstruct o and p also in a deep holographic regime in cone beam geometry (see figure 5(a)) relevant for high resolution x-ray imaging. Furthermore, LPCDI is well suited for high resolution imaging: the resolution of the reconstructed object is between 50 and 75 nm (half period) with low noise in the high frequency range (see power spectral density in figure 5(h) as well as selected horizontal and vertical profiles (i–j) for which error functions were adjusted to determine their steepness). We attribute the anisotropy in the resolution (see figure 5(h)–(j)) to beam fluctuations which are more pronounced in the vertical direction.

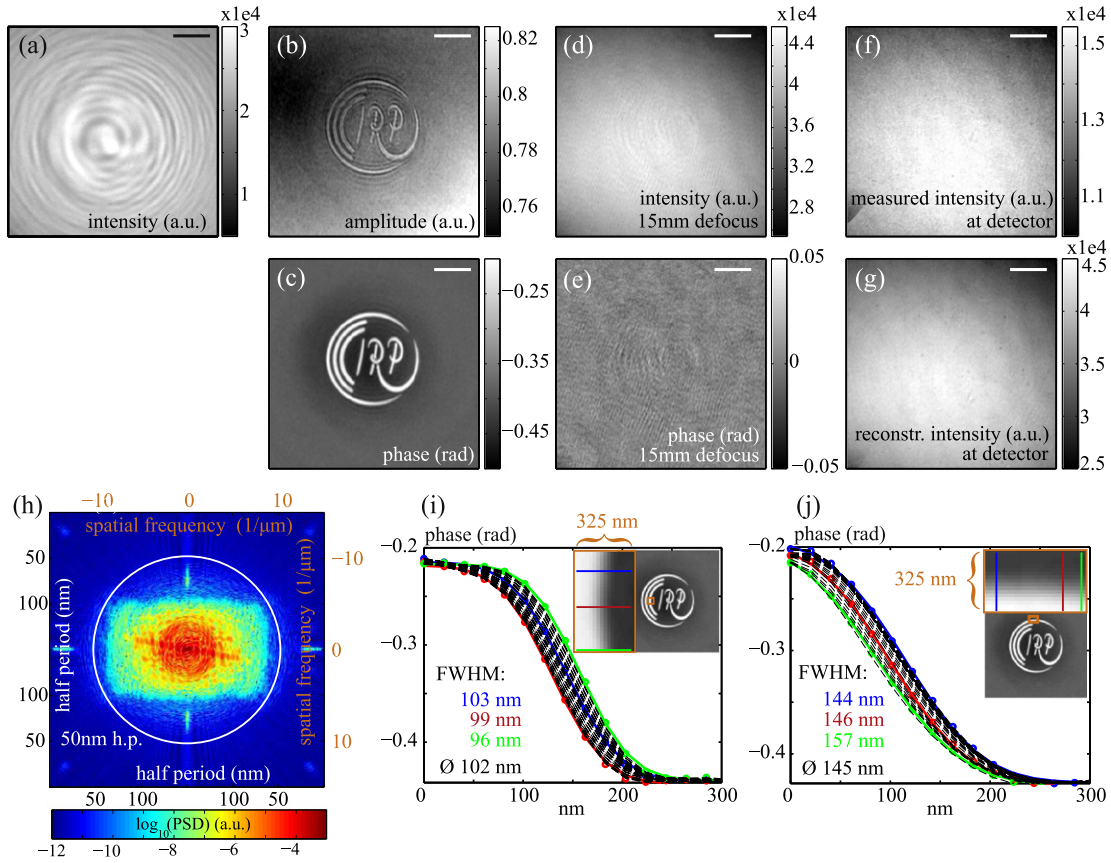

Figure 5. (a) An exemplary x-ray hologram of the test pattern recorded in the magnifying cone beam setup at DESY/P10. (b) Reconstructed amplitude of the object. (c) Reconstructed phase of the object. (d) Reconstructed intensity of the probe 15 mm behind the waveguide exit. (e) Reconstructed phase of the probe 15 mm behind the waveguide exit. (f) Measured intensity profile of the probe. (g) Reconstructed intensity profile of the probe at the detector. (h) Power spectral density of (c). (i) Selected horizontal cut; the full width at half maximum (FWHM) of the respective edges was determined by adjusting error functions. (j) Selected vertical cut; same analysis as in (i). Scale bars denote 2 μm.

4. Summary and conclusion

In summary, we have generalized ptychography to the near-field setting, enabling simultaneous probe and object reconstruction with extended beams, without the need for any wave front modification (for example by a diffuser). The necessary diversity in the data is generated by lateral *and* longitudinal shifts of the object in the beam. Importantly, the presented LPCDI approach overcomes the conventional linearizations of the object's transmission function or the propagation distance, as well as the inaccurate raw data correction scheme of dividing the measured holograms by the empty beam intensity pattern. In fact, no empty beam recordings are necessary at all. While near-field holography is *per se* compatible with a smaller spatial coherence length than far-field CDI [37], it is interesting to note that the present LPCDI approach could be directly enhanced by multi-modal reconstruction as shown for the far-field in [38]. For longitudinal (spectral) coherence the requirement of keeping the relative bandwidth small compared to the number of resolution elements can also be achieved easily [39]. The LPCDI method has been demonstrated experimentally for visible light and for x-rays, both in parallel and cone beam geometry. In particular, the example in figure 2 shows that reconstruction is successful even with strong phase shift of the object and large propagation, regardless of whether the probing wave front is nearly perfect or highly perturbed. Hence, it can also be used as a tool to characterize wave fronts in amplitude and phase.

As an outlook, we may speculate on whether LPCDI could also be used for super-resolution. In particular we consider the following setting: we are interested in the fine structure of an object, which diffracts components beyond the numerical aperture of the detector. This object in which we are ultimately interested in is now treated as a beam modulator. A specially designed 'reporter object' is placed downstream from this sample, close enough to ensure a high numerical aperture. The 'reporter object' is now designed in such a way that the waves encoding high spatial frequencies of the sample reach the detector. One may argue that such a reporter could very well be called an object lens. The difference, however, is that, augmented by phase retrieval, such a lens could be highly aberated without impeding clean reconstructions both of amplitude and phase. Many x-ray optics which

function well for focusing are not used as objective lenses, precisely due to these aberrations. It remains to be shown that the generalized ptychographic scheme of LPCDI presented here can provide clear and quantitative images for such settings.

Acknowledgments

We thankfully appreciate the support of M Krenkel, J Hagemann, M Töpperwien, A Ruhlandt and M Vaßholz during the ID19 beamtime and M Bartels, M Krenkel, M Osterhoff and M Sprung during the P10 beamtime. For help with the camera setup for the visible light experiment we thank A Ruhlandt and J Herbst. Financial support by the German Research Foundation (Deutsche Forschungsgemeinschaft, DFG) via SFB 755 is gratefully acknowledged.

References

[1] Gabor D 1948 *Nature* **161** 777–8
[2] Wilkins S W, Gureyev T E, Gao D, Pogany A and Stevenson A W 1996 *Nature* **384** 335–8
[3] Paganin D and Nugent K A 1998 *Phys. Rev. Lett.* **80** 2586–9
[4] Cloetens P, Ludwig W, Baruchel J, van Dyck D, van Landuyt J, Guigay J P and Schlenker M 1999 *Appl. Phys. Lett.* **75** 2912–4
[5] Mokso R, Cloetens P, Maire E, Ludwig W and Buffière Y-J 2007 *Appl. Phys. Lett.* **90** 144104
[6] Paganin D M 2006 *Coherent X-Ray Optics* (New York: Oxford University Press)
[7] Nugent K A 2010 *Adv. Phys.* **59** 1–99
[8] Quiney H M 2010 *J MOD. OPTIC.* **57** 1109–49
[9] Bronnikov A V 1999 *Opt. Commun.* **171** 239–44
[10] Krenkel M, Bartels M and Salditt T 2013 *Opt. Express* **21** 2220–35
[11] Giewekemeyer K, Krüger S P, Kalbfleisch S, Bartels M, Beta C and Salditt T 2011 *Phys. Rev.* A **83** 023804
[12] Paganin D M, Mayo S C, Gureyev T E, Miller P R and Wilkins S W 2002 *J. Microsc.* **206** 33–40
[13] Hagemann J, Robisch A-L, Luke D R, Homann C, Hohage T, Cloetens P, Suhonen H and Salditt T 2014 *Opt. Express* **22** 11552–69
[14] Homann C, Hohage T, Hagemann J, Robisch A-L and Salditt T 2015 *Phys. Rev.* A **91** 013821
[15] Guizar-Sicairos M and Fienup J R 2008 *Opt. Express* **16** 7264–78
[16] Thibault P, Dierolf M, Menzel A, Bunk O, David C and Pfeiffer F 2008 *Science* **321** 379–82
[17] Maiden A M and Rodenburg J M 2009 *Ultramicroscopy* **109** 1256–62
[18] Putkunz C T, Clark J N, Vine D J, Williams G J, Pfeifer M A, Balaur E, McNulty I, Nugent K A and Peele A G 2011 *Phys. Rev. Lett.* **106** 013903
[19] Stockmar M, Cloetens P, Zanette I, Enders B, Dierolf M, Pfeiffer and Thibault P 2013 *Sci. Rep.* **3** 1927
[20] Vine D J, Williams G J, Abbey B, Pfeifer M A, Clark J N, de Jonge M D, McNulty I, Peele A G and Nugent K A 2009 *Phys. Rev.* A **80** 063823
[21] Quiney H M, Peele A G, Cai Z, Paterson D and Nugent K A 2006 *Nat. Phys.* **2** 101–4
[22] Robisch A-L and Salditt T 2013 *Opt. Express* **21** 23345–57
[23] Faulkner H M L and Rodenburg J M 2004 *Phys. Rev. Lett.* **93** 023903
[24] Langehanenberg P, Kemper B and von Bally G 2007 *Proc. SPIE, Biophotonics 2007: Optics in Life Science (Munich)* 6633 66330E
[25] Onural L and Scott P D 1987 *Opt. Eng.* **26** 1124–32
[26] Voelz D G and Roggemann M C 2009 *Appl. Opt.* **48** 6132–42
[27] Born M and Wolf E 2002 *Principles of Optics* VII expanded edn (Oxford: Oxford University Press)
[28] Weitkamp T, Tafforeau P, Boller E, Cloetens P, Valade J P, Bernard P, Peyrin F, Ludwig W, Helfen L and Baruchel J 2010 *AIP Conf. Proc. (Karlsruhe, Germany)* 1221 33
[29] Labiche J-C, Mathon O, Pascarelli S, Newton M A, Ferre G G, Curfs C, Vaughan G, Homs A and Carreiras D F 2007 *Sco. Instrum. Rev.* **78** 091301
[30] Cerbino R, Peverini L, Potenza M A C, Robert A, Bösecke P and Giglio M 2008 *Nat. Phys.* **4** 238–43
[31] Kalbfleisch S, Neubauer H, Krüger S P, Bartels M, Osterhoff M, Mai D D, Giewekemeyer K, Hartmann B, Sprung M and Salditt T 2011 *AIP Conf. Proc. (Chicago, IL)* 1365 96
[32] Salditt T, Kalbfleisch S, Osterhoff M, Krüger S P, Bartels M, Giewekemeyer K, Neubauer H and Sprung M 2011 *Opt. Express* **19** 9656–75
[33] Neubauer H, Hoffmann S, Kanbach M, Haber J, Kalbfleisch S, Krüger S P and Salditt T 2014 *J. Appl. Phys.* **115** 214305
[34] Krüger S P, Neubauer H, Bartels M, Kalbfleisch S, Giewekemeyer K, Wilbrandt P J, Sprung M and Salditt T 2012 *J. Synchr. Rad.* **19** 227–36
[35] Bartels M, Priebe M, Wilke R N, Krüger S P, Giewekemeyer K, Kalbfleisch S, Olendrowitz C, Sprung M and Salditt T 2012 *Opt. Nanosc.* **1** 10
[36] Latychevskaia T and Fink H-W 2007 *Phys. Rev. Lett.* **98** 233901
[37] Claus D, Iliescu D and Rodenburg J M 2013 *Appl. Opt.* **52** 326–35
[38] Thibault P and Menzel A 2013 *Nature* **494** 68–71
[39] Salditt T, Giewekemeyer K, Fuhse C, Krüger S P, Tucoulou R and Cloetens P 2009 *Phys. Rev.* B **79** 184112